https://doi.org/10.1016/j.conbuildmat.2020.120844

In-situ X-ray microcomputed tomography monitoring of steel corrosion in engineered cementitious composite (ECC)

Qiwen Qiu [a], Jihua Zhu [b], Jian-Guo Dai [a,*]

[a] Department of Civil and Environmental Engineering, The Hong Kong Polytechnic University, Hong Kong, China

[b] College of Civil and Transportation Engineering, Shenzhen University, China

[*] Corresponding Author, Email: cejgdai@polyu.edu.hk

Abstract

Real-time and in-situ monitoring of the corrosion process of steel reinforcement covered by engineered cementitious composites (ECC) was conducted by using high-resolution X-ray microcomputed tomography. The test results revealed vividly that the corrosion-induced rusts fill into the pores near the steel and extend along the radial cracks towards the sample surface. Compared to plain mortar, ECC exhibits a few more microcracks and uniform crack distribution. While massive leaching of rust is found in the plain mortar, a significant amount of rust remains in the cracks of ECC. Through the image segmentation method, the volume loss of steel in ECC can be quantitatively monitored.

Keywords: engineered cementitious composite; durability; steel corrosion; cracking; X-ray microcomputed tomography; in-situ monitoring

1. Introduction

Many aged steel-reinforced concrete structures undergo reduction in structural integrity and loss of serviceability, due to the electrochemical corrosion of reinforcing steel bar [1-3]. Once the corrosion has initiated it yields rust that causes stresses within the concrete, leading to cracking and even spalling of structural concrete cover away from the steel reinforcement [4]. In concrete structures, steel corrosion is a major factor accelerating the material deterioration as well as the loss of load resistance. To improve the sustainability of steel-reinforced concrete structures, the use of high performance fiber reinforced cementitious composite (HPFRCC) for replacing conventional concrete cover has become a solution that provides the structure with better resistance against corrosion [5, 6]. ECC is a special class of HPFRCC and possesses excellent tensile ductility with the strain capacity in the range from 3% to 8% [7-9]. The high ductility of ECC is attributed to the fiber bridging effect in the cementing matrix [10, 11]. The role of fibers also leads to the formation of multiple and micro cracks in ECC in contrast to the few large cracks in ordinary Portland cement (OPC) concrete [12]. Due to the above characteristics, the use of ECC as the cover layer of OPC concrete structures has been increasingly applied [13, 14].

Although ECC holds great promise for providing steel-reinforced structures with physical protection and better durability, it is still a porous media which allows progressive penetration of aggressive substances (e.g. salt and moisture) from the external environment [15]. In other words, steel corrosion can still occur in ECC-covered steel-reinforced structures, resulting in formation of cracking in ECC. Recently, researchers have discovered that cracked ECC has less resistance to the penetration of gas, water and chloride ions [16-18]. Therefore, understanding the corrosion process of steel reinforcement and its induced cracks in ECC is important for the structural

71 durability design. A previous study revealed that at least ten corrosion-induced
72 microcracks (< 0.1 mm) were formed on the ECC surface, in comparison to a large
73 longitudinal crack observed on OPC concrete surface [19]. In general, the crack width
74 of OPC concrete keeps increasing with the evolution of corrosion [20]. In contrast to
75 the OPC concrete with "localized" macro-cracks, when the internal steel corrodes, ECC
76 remains nearly the constant tight crack width and exhibits a significant anti-spalling
77 ability [21]. Yet, the underlying mechanism of corrosion-induced cracking process in
78 ECC has been rarely clarified. It is considered that corrosion-induced cracking is
79 interacted with rust production and expansion, pore filling effect, pore deformation,
80 fiber bridging, and rust infiltration into crack space. It is also thought that the cracking
81 behavior is closely related to the type of fibers mixed in ECC [22, 23]. An experimental
82 and non-destructive monitoring of multi-phase evolutions related to steel corrosion in
83 ECC can thus benefit the development of predictive corrosion-induced crack models in
84 ECC. Furthermore, a comprehensive understanding of corrosion process and its
85 induced cracking in ECC also benefits an optimal material design towards a more
86 durable ECC application in reinforced concrete structures.
87 Traditionally, the ink injection method, scanning electron microscope (SEM), and
88 optical microscopy have been used for tracing existing cracks in concrete and other
89 cementitious materials [24-27]. However, these methods need destructing the test
90 sample during the observation (i.e., after stopping the corrosion) and thus cannot
91 capture the continuous crack development in a single test sample. It is not possible to
92 trace dynamically how the cracking is initialized and how the multiple phases (e.g. rust,
93 pore) evolve and interact with each other during the corrosion process. The advantage
94 of high-resolution X-ray microcomputed tomography (X-ray μCT) has proven to be an
95 excellent means for in-situ and real-time monitoring of morphological, structural, and

topological changes in a material system, and elucidation of their underlying mechanism [28]. Recently, some studies had demonstrated that X-ray μCT has an ability to visualize the pore structure of cementitious composites [29-31]. The pore size distribution in hardened cement paste could be quantitatively determined through X-ray μCT integrated with metal centrifugation porosimetry [32]. Besides, the evolution of pore structure during hydration of tricalcium silicate was visualized in a recent study [33]. The CT scanning was also applied for observing the damage of cement mortar under freeze and thaw actions. Based on the X-ray μCT data, a damage model of elasticity modulus of cement mortar was established and validated by the experimental results [34]. Furthermore, X-ray μCT has been confirmed to be a potential tool for studying cracking characteristics [35-37] and other aspects [38-40] of cement and concrete materials.

The present research aims to investigate the corrosion process of steel embedded in ECC matrix for the first time and its induced cracking process through the X-ray μCT, particularly in terms of the complex interaction between corroded steel and surrounding ECC matrix. Two common types of ECC, namely the polyvinyl alcohol fiber-reinforced engineered cementitious composite (PVA-ECC) and the polyethylene fiber-reinforced engineered cementitious composite (PE-ECC), were investigated. OPC mortar was prepared as a reference system without fibers.

2. Experimental program

2.1 Material systems

Three material systems, namely conventional plain cement mortar, PE-ECC and PVA-ECC, which surrounded a corroding steel rod, were considered for this study. The conventional plain mortar was made as a regular cementing mixture with coarse sand

that does not contain fibers to be the reference. In practice, both polyvinyl alcohol (PVA) fiber and polyethylene (PE) fiber are commonly utilized to produce ECC, while they can lead to different ductility and cracking behavior of material in tension. Considering the fiber type affects corrosion-induced cracking, both PE-ECC and PVA-ECC were investigated. Table 1 lists the detailed mixture proportions of these three material systems. The ECC was synthesized with type I OPC, Class C fly ash, silica sand, fiber and superplasticizer. Besides, the PVA fiber had the density of 1.300 g/cm^3, the tensile strength of 1600 Mpa, the elastic modulus of 48 GPa, the diameter of 40 μm, and the length of 12 mm. The PE fiber had the density of 0.970 g/cm^3, the tensile strength of 3000 MPa, the elastic modulus of 114 GPa, the diameter of 17 μm, and the length of 13 mm. The total fiber volume fraction for PE-ECC and PVA-ECC was both fixed at 2%. The fine silica sand was adopted for producing both ECCs and had a maximum 212 μm grain size, in accordance with the previous research work [41]. A high-range water reducing agent (i.e., MasterRheobuild 1100 from BASF) was used as the superplasticizer for both PE-ECC and PVA-ECC fabrications.

Table 1

Mixing proportion of mortar, PVA-ECC and PE-ECC.

Items	Mortar	PVA-ECC	PE-ECC
	Mixing proportion		
Fly ash/cement	0	1.2	1.2
Water/binder	0.26	0.26	0.26
Sand/cement	0.36	0.36	0.36
Water (Kg/m^3)	361.6	365.0	365.0
Cement (Kg/m^3)	1390.9	638.0	638.0

Fly ash (Kg/m^3)	0	765.6	765.6
Sand (Kg/m^3)	500.7	229.7	229.7
Superplasticizer (Kg/m^3)	0	19.1	19.1
PVA or PE fiber (Kg/m^3)	0	26	19.4

Note: The plain mortar specimens were adjusted to have similar mechanical strength with the ECC specimens. However, the low sand/binder ratio was used for the specimens to facilitate easier filling of fresh mixture into the small steel-inserted mould and compacting on vibrating table.

During ECC fabrication, the solid ingredients, including cement, fly ash and silica sand were first mixed for a period of approximately 2 minutes in a slow speed. Then, tap water was weighed, added and mixed into the precursor materials for another 4 minutes prior to the addition of superplasticizer. Incorporating fibers into the mixture was then conducted. It is worth mentioning that air pressure was applied to separate the bundles of fibers, with the aim of achieving good dispersion of fibers into the mixture following the previous literature [41, 42]. The whole mixing time took about 16 minutes. After mixing, all fresh mixtures were compacted via a mechanical vibrating table and cast in molds. A plastic film was used to cover the molded specimens for 24 hours in order to avoid cracks caused by dry shrinkage. After demolding, all specimens were cured in a moist condition (at 100% humidity and room temperature 20 ^oC) for the following 27 days before the accelerated corrosion test. Regarding the mechanical tests, specimens for both 7- and 28-days curing periods were fabricated.

2.2 Mechanical tests

PE-ECC and PVA-ECC, cube specimens and dogbone-shaped specimens were

fabricated for compressive and tensile loading tests, respectively. The ECC cube specimens had the dimensions of 50 mm × 50 mm × 50 mm. Three identical specimens were tested for each type of material system and each type of mechanical loading and the results were averaged. Compressive strength of cube specimens of plain mortar, PE-ECC and PVA-ECC was determined in accordance with ASTM C109 [43]. Uniaxial tension tests were conducted in accordance with the recommendation of Japan Society of Civil Engineers (JSCE) [44] and ASTM C1273-05 [45]. The tensile tests were conducted using universal testing machine where the load was applied by displacement control with a rate of 0.5 mm/min. Two linear variable differential transducers (LVDTs) were placed at both sides of dogbone-shaped specimen to measure the elongation over a gauge length of 80 mm, as shown in Fig. 1, to obtain the tensile strain. The tensile stress was obtained by dividing the load by the cross-section of the specimen. As a result, the tensile stress-strain curve of ECC was yielded.

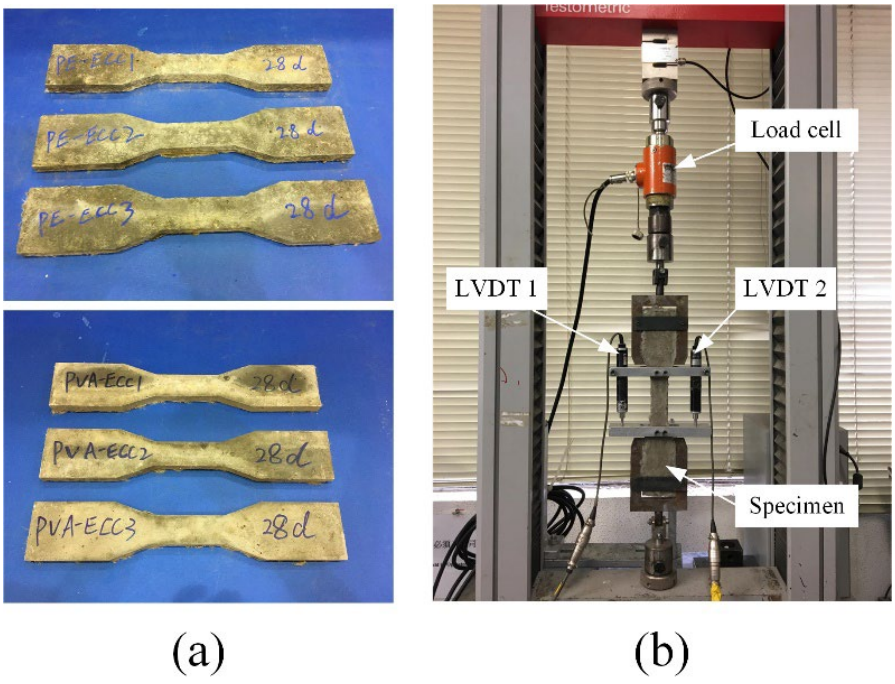

Fig. 1. Tensile tests: (a) dogbone-shaped specimens and (b) loading setup.

176

177 *2.3 Accelerated steel corrosion test*

178 Besides the aforementioned specimens for mechanical loading tests, steel-inserted
179 mortar (S-M), steel-inserted PE-ECC (S-PE-ECC) and steel-inserted PVA-ECC (S-
180 PVA-ECC) were fabricated for accelerated corrosion test and X-ray μCT scanning. All
181 specimens were cylinders with a centrally placed steel rod and had the same dimension,
182 as illustrated in Fig. 2(a). Prior to specimen casting, the weight of steel rod was
183 measured and recorded for quantifying the mass loss due to corrosion. In order to
184 fabricate the cylindrical steel-inserted sample, a special silica gel mould was designed
185 where the steel rod could be easily inserted at first and then the mortar mixture was
186 filled, as illustrated in Fig. 2(b). The curing condition of steel-inserted samples was 100%
187 humidity and 20 °C. During the curing process, epoxy resin was coated on the steel
188 outside the cylinder with the purpose to prevent corrosion. For each type of material
189 system, three identical samples were made in the experiment. Fig. 2(c) gives the
190 photographs of steel-inserted samples after demolding and curing.

191

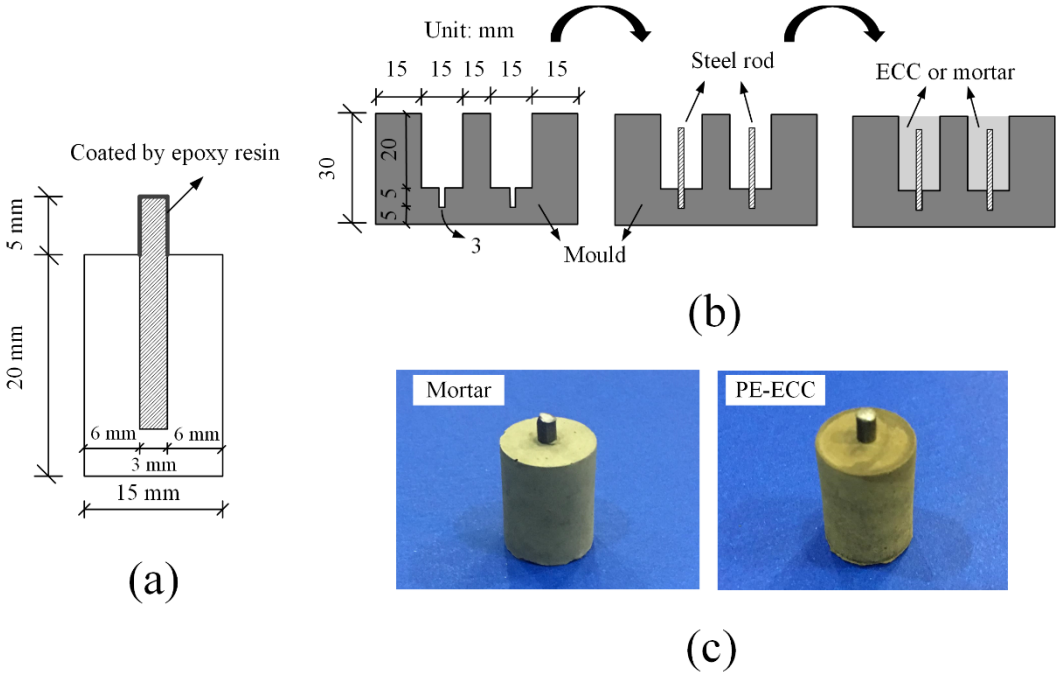

192

193 Fig. 2. Sample preparation for accelerated corrosion test and X-ray μCT scanning: (a)
194 dimension of steel-inserted cylindrical sample, (b) schematic representation of silica
195 gel mold for casting of steel-inserted cylindrical sample, and (c) photograph of steel-
196 inserted mortar and steel-inserted ECC.
197
198 Accelerated steel corrosion, based on the electrolyte corrosion technique, was
199 employed to investigate the corrosion-induced cracking in plain mortar, PE-ECC and
200 PVA-ECC. In this accelerated corrosion scheme, both the cylindrical specimen and the
201 copper bar (as a counter electrode) were immersed into a 5% NaCl solution, as depicted
202 in Fig. 3(a). The exposed part of the steel rod was connected to the positive terminal of
203 a power source, and the top end of the copper bar was linked to the negative terminal.
204 Such corrosion test scheme was widely used in previous studies [19, 35, 46, 47]. In the
205 present test, the accelerated corrosion process was carried out by supplying a constant
206 current of 0.001 A (i.e. corresponding current density of around 530 $\mu A/cm^2$). Such
207 level of output current density was commonly adopted and could effectively induce the
208 steel corrosion [35, 48], while the test period could be reasonably shortened. A
209 computer program was used to control the output current and the testing duration.
210 Additionally, the total corrosion process started from 0 to 3000 minutes. Fig. 3(b) gives
211 the photographs of the setup of accelerated corrosion test.
212

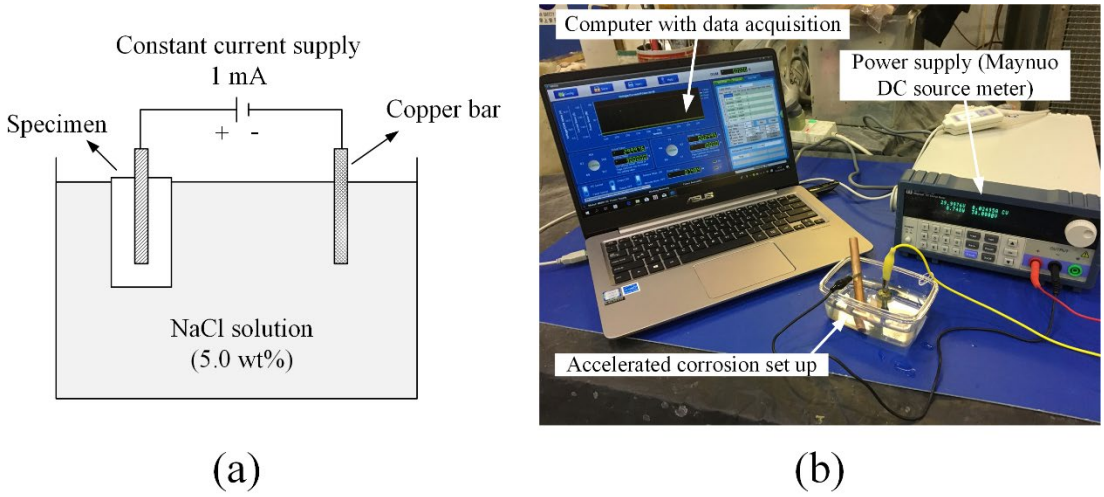

Fig. 3. Accelerated corrosion test for S-M, S-PE-ECC, and S-PVA-ECC: (a) schematic representation of accelerated corrosion test, and (b) photograph of setup of accelerated corrosion test.

2.4 X-ray μCT scanning

X-ray μCT probes the attenuation of X-rays transmitting through a material at 360º orientation, thereby reconstructing the cross-sectional radiographs that exhibit the spatial distribution of linear attenuation coefficient of the material under research [49]. The amplitude of linear attenuation coefficient is correlated with chemical composition of material system and the emitted X-ray energy. X-ray μCT had been considered as an advanced characterization technique that can yield high-resolution representation of internal physical phases within porous media. In the present research work, S-M, S-PE-ECC and S-PVA-ECC at the accelerated corrosion periods of 0, 1000, 2000 and 3000 minutes were scanned by X-ray μCT instrument. The X-ray μCT facility mainly encompassed a microfocus X-ray transmitter, a receiver equipped with three multiple charge-coupled device (CCD) cameras, a 360° rotation stage for supporting specimen, and a computer program for data acquisition and analysis. Fig. 4(a) gives the schematic diagram of test principle of using X-ray μCT for material characterization. In addition,

Fig. 4(b) shows the arrangement of specimens and core devices in the X-ray μCT instrument. Planar X-rays were transmitted towards the sample, and some X-rays were absorbed. The un-absorbed portion of X-rays was then received by X-ray detector. The sample experienced a 360-degree rotation so that a slice of radiograph showing the two-dimensional CT data was generated. In addition, the sample was shifted in the vertical direction step by step to acquire a set of slices. Stacking these image slices with a computational software was conducted to reconstruct the three-dimensional (3D) image of the sample under investigation.

In order to get a high-resolution tomogram with the image size of 1012 × 1024, the X-ray source excitation voltage and current were set as 85 kV and 117 μA, respectively. In addition, the optical magnification factor was set as 0.39, and the beam hardening value was set as 0.15 during reconstruction. It is also worth noting that the pixel size scanned by X-ray μCT technique is dependent of the dimension of specimen (i.e. 15-mm diameter and 25-mm height). For scanning the whole specimen configuration, the corresponding pixel size down to 26.615 μm was adopted.

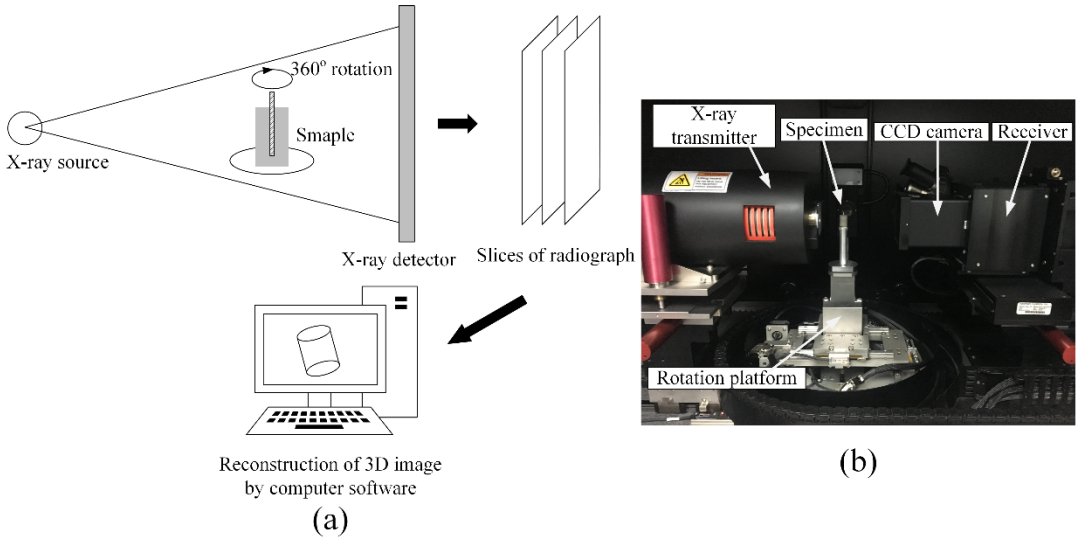

Fig. 4. X-ray μCT scanning scheme: (a) principle of using X-ray μCT for material characterization and (b) photograph of sample and core instruments in X-ray μCT

scanning machine.

3. Results and discussion

3.1 Compressive and tensile properties of plain mortar, PE-ECC and PVA-ECC

The mechanical properties of plain mortar, PE-ECC and PVA-ECC were tested after 7- and 28-day curing, respectively. Both the compressive and tensile properties were tested, as described in Figs. 5(a) and (b). It is seen that the compressive strength and the first cracking strength of plain mortar were slightly higher than those of ECC mixtures. However, the tensile strengths showed an opposite trend, as shown in Fig. 5(d). The increased tensile strength of ECC could be attributed to the role of fibers that bridged the cementitious matrix and brought about the strain-hardening effect. Besides, the ultimate tensile strain of 28-day cured ECC could reach over 3% (Fig. 5(e)), while the tensile strain of all plain mortar specimens was too small to be measured by LVDTs. Generally, ECC possesses a strain capacity several hundred times greater than that of normal OPC concrete, as documented in literature [5, 50]. Moreover, it is seen that both PE-ECC and PVA-ECC exhibited the strain-hardening behavior along with the multiple cracking characteristic under the tensile loading. Based on the observation of specimen after tensile failure, PE-ECC exhibited higher ductility and wider crack width compared to PVA-ECC. This difference is associated with the difference of hydrophilic properties between the PVA and PE fibers. In PVA-ECC, a strong frictional bonding between the fiber and matrix can be formed due to the hydrophilicity of PVA fiber [51, 52]. The strain capacity of PVA-ECC in the cracking process under tensile loading is limited, in comparison to that of PE-ECC. In the tensile stress-strain curve (see Figs. 5(f) and (g)), the strain capacity of PVA-ECC was about 3-4% while the strain capacity of PE-ECC exceeded 6%. The excellent strain capacity of ECC using PE fibers was also

demonstrated in previous studies [7, 23, 53].

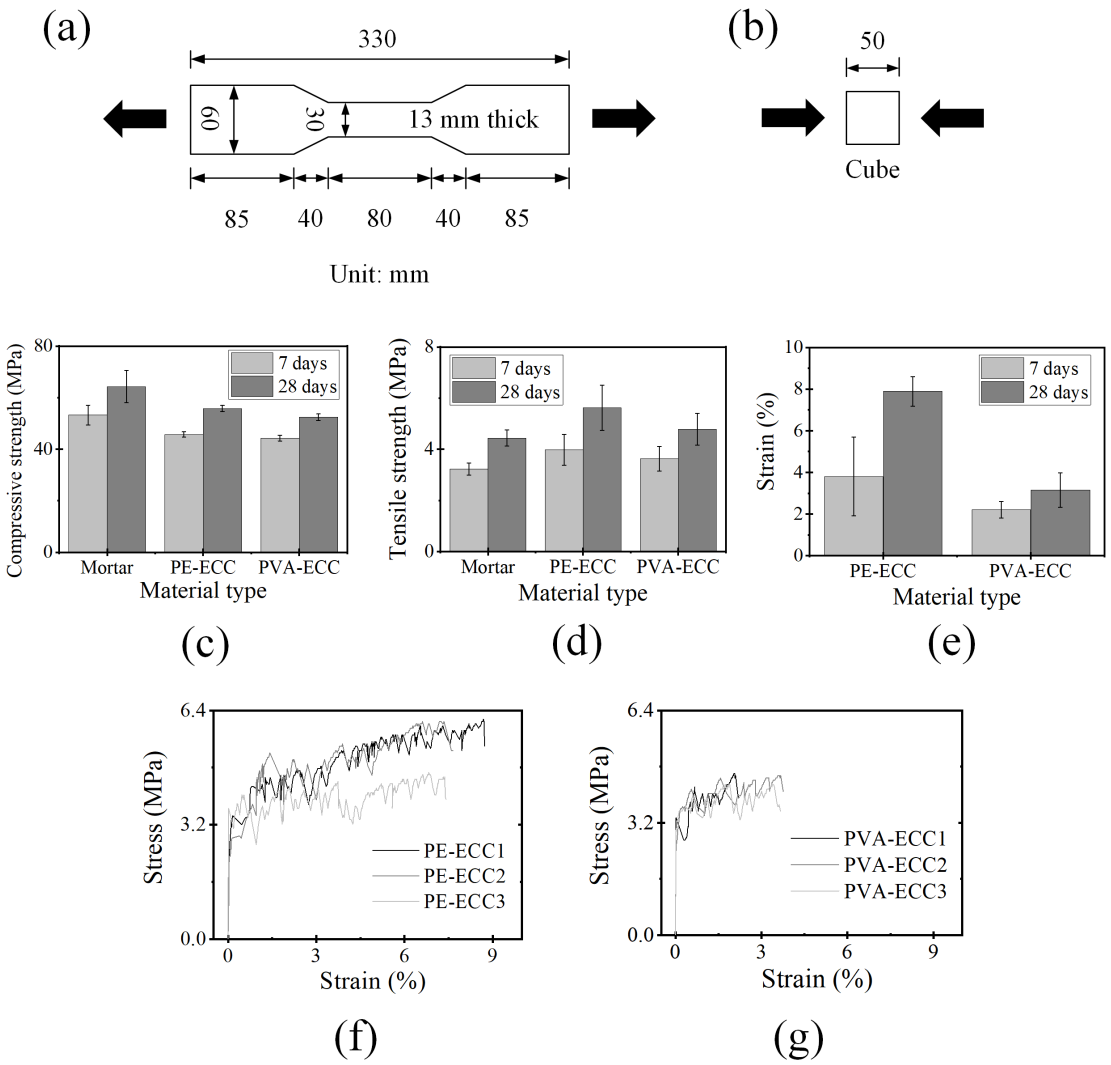

Fig. 5. Compressive and tensile properties of plain mortar and ECCs: (a) schematic diagram of dogbone-shaped specimens for uniaxial tensile loading test, (b) schematic diagram of cube-shaped specimens for compressive loading test, (c) compressive strength, (d) tensile strength, (e) elongation, (f) tensile stress-strain curves of PE-ECC, and (g) tensile stress-strain curves of PVA-ECC.

3.2 In-situ monitoring of corrosion and its induced cracking

All of S-M, S-PE-ECC and S-PVA-ECC samples were subjected to the same

accelerated corrosion condition for comparing their corrosion resistance and cracking process. At the corrosion durations of 0, 1000, 2000 and 3000 minutes, the samples were scanned by the X-ray μCT technique. Fig. 6 displays the two-dimensional gray-scale images of S-M, S-PE-ECC and S-PVA-ECC at different stages. To geometrically align CT scanned images at different corrosion periods, the image registration was conducted by feature matching and aligning a characteristic surface hole of the sample before corrosion. In these tomograms, voids, cracks, aggregates, cement paste, rust and steel are identified by different gray-scale colors. The gray-scale color reflects the atomic density intrinsic to each substance. The white color indicates the most highly X-ray-attenuating material (i.e. steel) and the black color indicates the least attenuating one (i.e. air). The rust is highly X-ray-attenuating and displayed as bright grey around the steel rod, given that the corrosion product is in the form of fine particles of various iron oxyhydroxides and oxides. Consequently, direct qualitative evaluation on the corrosion-induced rust and cracking characteristics in the raw CT images can be achieved.

As the corrosion proceeds, the rust was found to accumulate around the surface of steel rod. During the early corrosion period, the rust filled into the pores in the vicinity of steel (e.g. pore 3 in S-M, pore 7 in S-PE-ECC and pore 7 in S-PVA-ECC). Such observation coincides with the previous studies [54-56]. This phenomenon can be associated with the continuous rust accumulation that causes internal expansive stress. Due to the rust expansion, the steel corrosion induced cracks in plain mortar, PE-ECC as well as PVA-ECC. From the observation of tomograms in Fig. 6, the cracks tended to occur from the filled pores and then propagated radially towards the sample surface. During the crack propagation, the rust could even fill into the crack space (e.g. crack 2 in S-M and crack 2 in S-PE-ECC). Such rust filling promoted the movement of crack

front towards the sample surface. Also, the rust filling also resulted in wider opening of cracks, and this effect was more remarkable in plain mortar. Once the crack arrived at the sample surface, the rust migrated outside and diffused into the external NaCl solution.

Under steel corrosion, all the cylindrical S-M, S-PVA-ECC and S-PE-ECC samples presented radial cracks initiated from the central steel bar, but their propagation paths were different. It is interesting to find that crack (e.g. crack 1 of S-M) in plain mortar was prone to extend into the interfacial transition zone (ITZ) between the aggregate and the cement paste, which is usually regarded as the weakest region in mortar and concrete [57, 58]. This behavior resulted in tortuous shape of crack in the plain mortar. Nevertheless, such cracking behavior was not evident in the ECC material system where the ITZ was densified due to the use of finer sand for ECC mixture.

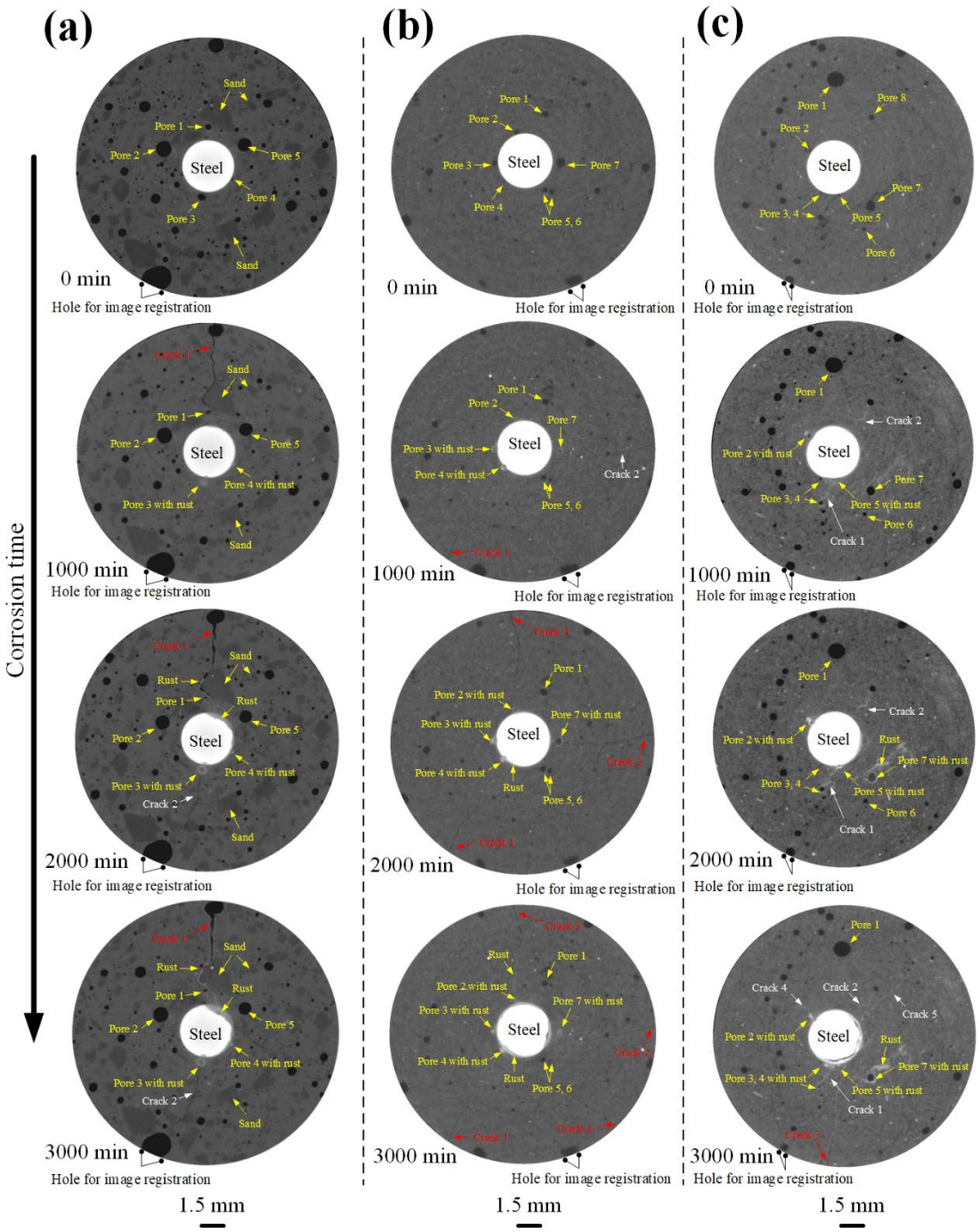

Fig. 6. Two-dimensional gray-scale images (gray-scale value ranges from 0 to about 65500) of three material systems: (a) S-M, (b) S-PE-ECC, and (c) S-PVA-ECC.

As previously discussed in section 3.1, both PE-ECC and PVA-ECC showed the strain-hardening behavior and multiple cracking compared to plain mortar. The difference of mechanical properties between mortar and ECCs gives rise to their variation in crack

growth during the corrosion process. Overall, during the corrosion process, ECCs exhibited smaller crack widths and larger number of cracks than plain mortar. The similar observation was found in another set of specimens of S-M, S-PE-ECC and S-PVA-ECC at the corrosion time of 3000 minutes, as shown in Fig. 7. The behavior was also confirmed in reinforced ECC structural members subjected to steel corrosion [33, 59]. Furthermore, in comparison to S-PVA-ECC, S-PE-ECC exhibits more cracks that extended to sample surface (highlighted with red in Figs. 6 and 7). This result can be reflected and elucidated by the difference of tensile strain between PE-ECC and PVA-ECC, as shown in Fig. 5.

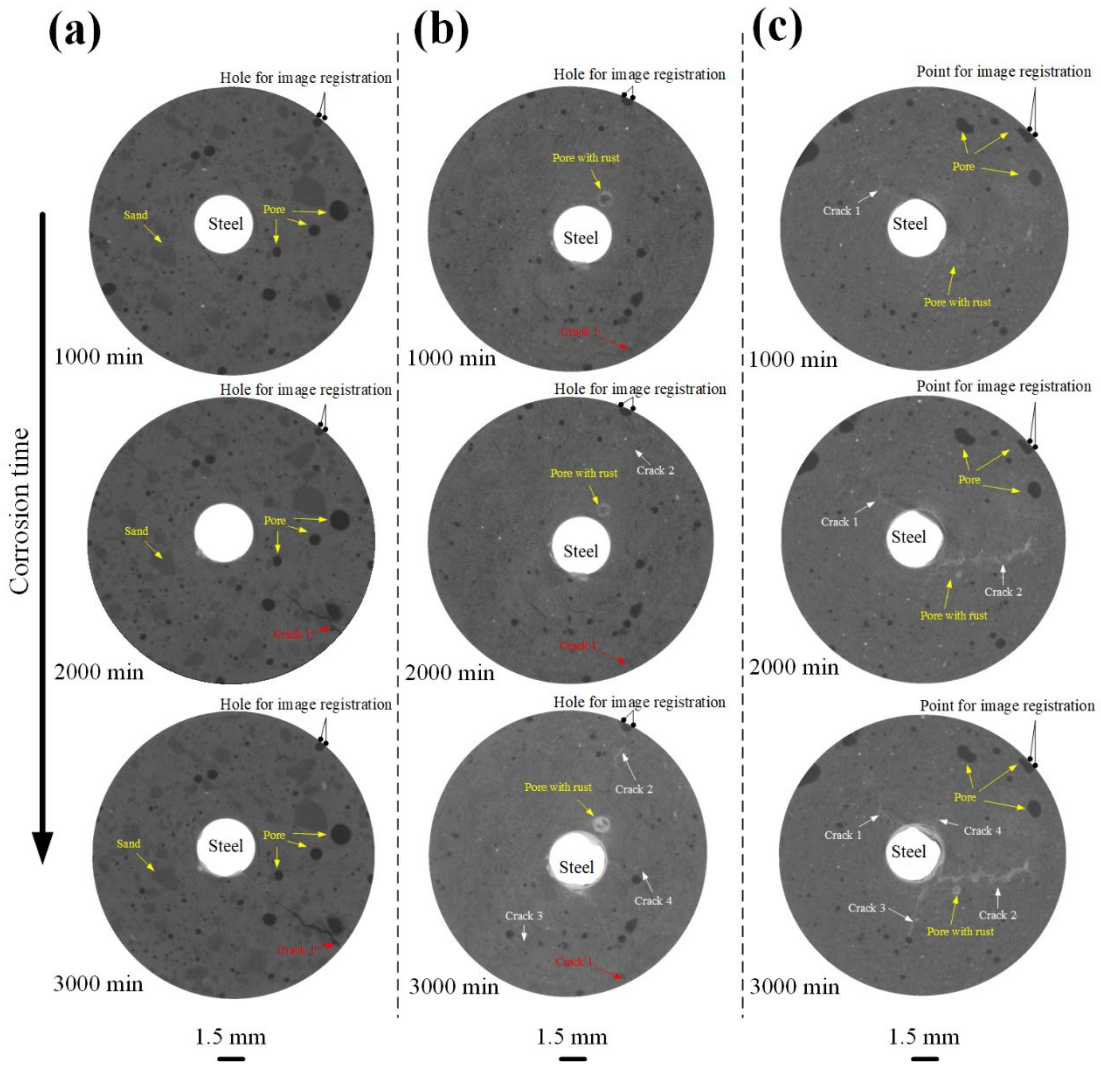

Fig. 7. Two-dimensional gray-scale images of other reproduced specimens at 1000, 2000, and 3000 minutes' corrosion time: (a) S-M, (b) S-PE-ECC, and (c) S-PVA-ECC.

3.3 Quantitative estimation of corrosion process and its induced cracking

With the time-series of tomograms scanned by X-ray μCT, it is possible to quantitatively analyze the corrosion process and its induced cracking characteristics. In this study, the physical characteristics of the mass loss of steel rod and the crack width inside the material were quantitatively investigated. To perform the quantitative analysis, image segmentation was commonly used to separate an image into different discrete phases (e.g. steel, cracks and cementitious material) and estimate the volume of each phase [60, 61]. The image segmentation technique determines the grey-scale threshold intrinsic to a region of interest (ROI) and outputs the discrete ROI where pixels within the threshold are added while others are removed [49, 62, 63]. By the aid of image segmentation technique, the volume of steel component at a specific corrosion period of t can be estimated as:

$$\mathrm{V}_{image(t)} = N \times S \qquad (1)$$

where $V_{image(t)}$ denotes the image-estimated steel volume at corrosion time t, N denotes the number of spatial voxels, S denotes the spatial voxel size. Hence, the mass loss of steel during different corrosion stages can be estimated by the following equation:

$$\Delta m_{image(t)} = (\mathrm{V}_{image(0)} - \mathrm{V}_{iamge(t)}) \times \rho_{steel} \qquad (2)$$

where $\Delta m_{image(t)}$ denotes the image-estimated mass loss of steel at corrosion time t,

368 $V_{image(t)}$ denotes the image-estimated steel volume at steel corrosion time t, $V_{image(0)}$
369 denotes the image-estimated steel volume before steel corrosion, ρ_{steel} denotes the
370 density of steel. To validate the reliability of estimated result from the image-based
371 processing technique, the mass loss of steel was also theoretically determined by
372 Faraday's Law, as expressed in equation (3). Experimental measurement of actual mass
373 loss was also conducted for comparison with the above two types of predicted results.
374
375 $$\Delta m_{theoretical(t)} = \frac{M}{zF} \times It \qquad (3)$$
376
377 In equation (3), $\Delta m_{theoretical(t)}$ denotes the theoretically calculated mass loss (g) of steel
378 at corrosion time t (seconds), M denotes the atomic weight of steel (56 g/mol), I denotes
379 the corrosion current (A), z denotes the number of valence electrons (2 for steel), F
380 denotes the Faraday's constant (F = 9.6487 × 10,000 C/mol). In the experimental
381 measurement of steel mass loss, specimens S-M, S-PE-ECC and S-PVA-ECC were
382 broken to acquire the steel rod after the whole process of accelerated corrosion test. For
383 each type of specimen, the steel rod was cleaned by deionized water, dried under 40 °C,
384 and scrubbed by a stiff metal brush to get rid of adhering corrosion products on the steel
385 surface. Then, the steel rod was weighed, and the mass loss could be calculated as
386 follows:
387
388 $$\Delta m_{experimental(t)} = m_{experimental(0)} - m_{experimental(t)} \qquad (4)$$
389
390 where $\Delta m_{experimental(t)}$ denotes the experimentally measured mass loss of steel at
391 corrosion time t, $m_{experimental(t)}$ denotes the measured mass of steel at corrosion time t,
392 and $m_{experimental(0)}$ denotes the measured mass of steel before steel corrosion. The

393 measurement procedures of mass loss of steel can also be referred to previous study
394 [19]. Apart from the steel mass loss, the crack width at the sample surface was directly
395 captured by the scanned CT images for quantitative analysis.
396 As shown in Fig. 8, before corrosion, a plain surface was seen on the steel rod in three
397 types of specimens. After the corrosion initiated, the morphology of steel surface was
398 clearly found to have significant changes. Based on the observation of corroded steel
399 surface, it is shown that concave holes on the steel surface in S-PVA-ECC and S-PE-
400 ECC were smoother than those in S-M. In S-M, a local deep hole was formed at the
401 surface of steel. This might reflect the quasi-brittle nature of mortar that led to few,
402 large and local crack opening during the process of steel corrosion. When the cracking
403 propagated to the mortar surface, the wide crack opening facilitated the leaching of rust.
404 Under this circumstance, steel was more vulnerable to the electrochemical corrosion at
405 the cracked region. On the contrary, the formation of smoother concave steel surface in
406 ECC indicated that the corrosion products as well as cracks were more evenly
407 distributed around the sample. Based on the ROI of steel rod, the number of its voxels
408 could be determined. Given the size of voxel obtained in X-ray μCT, the steel volume
409 was thereby quantified. Fig. 8 shows the loss ratio of steel volume in S-M, PVA-ECC
410 and PE-ECC after 0, 1000, 2000, and 3000 minutes of accelerated corrosion. With the
411 image-estimated steel volume, the mass loss of steel rod due to corrosion could be
412 obtained.
413

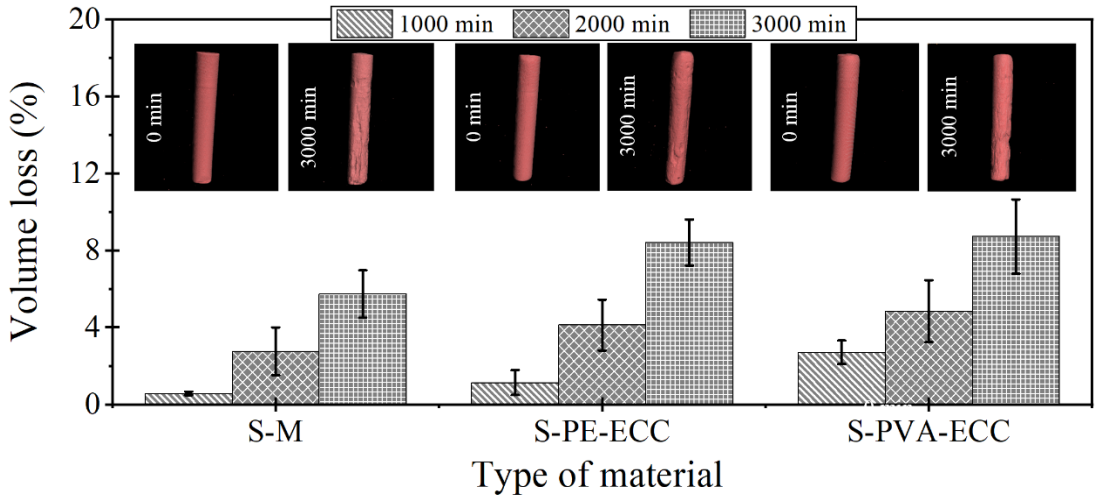

Fig. 8. Image-based analysis of steel surface morphology and estimation of steel volume loss in ratio for S-M, S-PE-ECC and S-PVA-ECC at different corrosion periods of 1000, 2000, and 3000 minutes.

In order to examine the results of mass loss calculated from the image-based technique, the theoretical value predicted based on equation (3) and the mass loss experimentally weighed in the laboratory. Fig. 9 shows the loss ratio of steel mass for S-M, S-PVA-ECC and S-PE-ECC before and after corrosion, from the theoretical calculation, weight measurement and image-based analysis. The comparison shows that the prediction from CT image-based analysis was in acceptable agreement with the theoretical one. The actual measurement shows a slightly large deviation from the theoretical one particularly in case of PVA-ECC probably because the rust removal process had some uncertainty, especially the steel rod length embedded in the mortar/ECC matrix was short, which might enlarge such deviation.

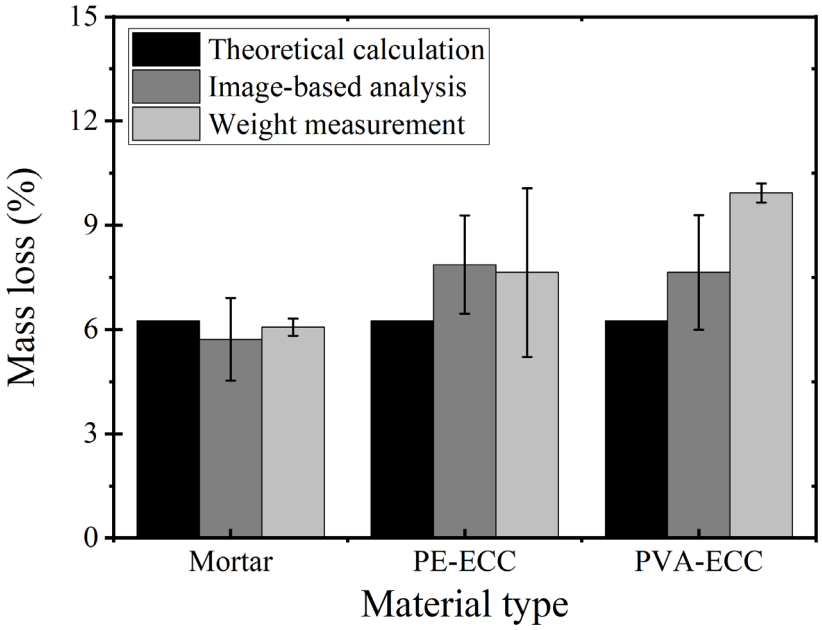

Fig. 9. Image-based estimation of steel mass loss at corrosion time of 3000 minutes.

In addition to the mass loss of steel rod, the evolution of surface crack width of plain mortar and ECCs was quantitatively compared in Fig. 10, where the PVC-ECC specimen is not included because there was almost no surface crack observed. As seen in Fig. 10, the surface crack width in S-M increased with the corrosion time, while the increasing rate was reduced as the corrosion proceeded further. The less increment of mortar's crack width is attributed to the rust leaching outside the crack space so that the rust expansion stress in the old crack was reduced. Compared to the plain mortar, the PE-ECC specimen had much smaller surface crack width. In particular, at the corrosion time of 3000 minutes, the variation of crack width of PE-ECC was much less than that in the case of plain mortar. This indicates that ECC features more uniform crack width. It is also clear that the crack width of PE-ECC tended to reduce slightly in the later corrosion process, which could be attributed to the rust precipitation at that time.

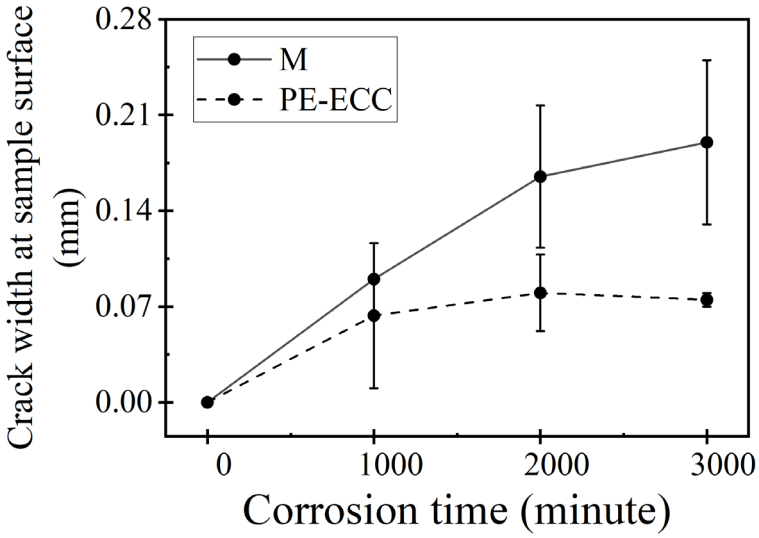

Fig. 10. Quantitative analysis of crack widths at the surface of S-M and S-PE-ECC samples with different corrosion time.

4. Conclusions

The in-situ process of steel corrosion and its induced cracking in both plain mortar and ECC were investigated by high-resolution X-ray μCT, to achieve an in-depth understanding of the morphological, structural, and topological changes of different phases (i.e. rust migration, crack propagation, and variation of steel surface morphology) during the process of steel corrosion. Through the research the following conclusions can be drawn up:

1. For both plain mortar and ECC, steel corrosion in early period causes rust filling into the pores in the vicinity of steel rod. Besides, the rust product induces cracking in plain mortar, PE-ECC and PVA-ECC. The corrosion-induced cracks tend to extend from pores filled with rust and propagate in a radial direction towards the sample surface. As the corrosion proceeds, rust fills into the crack space and continuously migrates outside.
2. Cracking characteristics between plain mortar and ECC are quite different. In steel-inserted mortar, corrosion induced cracking tends to occur locally at the ITZ between

aggregate and cement paste. The resultant crack width is relatively large, allowing massive leaching of rust. In contrast, ECCs with corroded steel rod experiences longstanding growth of tiny and uniformly distributed cracks during the corrosion process. Compared to PVA-ECC, cracks in PE-ECC are more likely to propagate to the sample surface.

3. Crack width in ECCs increases in the early corrosion period, while even reduces slightly at the later corrosion period due to rust precipitation at the crack space.
4. Quantitative analysis of corrosion process (i.e. steel mass loss and crack width variation) in plain mortar and ECCs can be efficiently conducted in the scanned tomograms. Estimation of steel mass loss from image segmentation method is in acceptable agreement with those obtained by theoretical prediction.

Acknowledgements

The authors are grateful for the financial support received from Chinese Guangdong Province R&D Plan for Key Areas (2019B111107002), the Hong Kong RGC Theme-based Research Scheme (T22-502/18-R), and the Postdoctoral Hub Scheme of Hong Kong Innovation and Technology Fund (Project code: PiH/176/19).

References

[1] C.L. Page, Mechanism of corrosion protection in reinforced concrete marine structures, Nature 258(5535) (1975) 514–515.

[2] J. Cairns, G.A. Plizzari, Y. Du, D.W. Law, C. Franzoni, Mechanical properties of corrosion-damaged reinforcement, ACI Mater. J. 102(4) (2005) 256-264.

[3] F.P. Glasser, J. Marchand, E. Samson, Durability of concrete-degradation phenomena involving detrimental chemical reactions, Cem. Concr. Res. 38(2) (2008)

226-246.

[4] Y. Chen, C. Xia, Z. Shepard, N. Smith, N. Rice, A.M. Peterson, A. Sakulich, Self-healing coatings for steel-reinforced concrete, ACS Sustainable Chem. Eng. 5(5) (2017) 3955-3962.

[5] V.C. Li, On engineered cementitious composites (ECC), J. Adv. Concr. Technol. 1(3) (2003) 215-230.

[6] M. Sahmaran, O. Anil, M. Lachemi, G. Yildirim, A.F. Ashour, F. Acar, Effect of corrosion on shear behavior of reinforced engineered cementitious composite beams, ACI Mater. J. 112(6) (2015) 771-782.

[7] K.-Q. Yu, J.-T. Yu, J.-G. Dai, Z.-D. Lu, S.P. Shah, Development of ultra-high performance engineered cementitious composites using polyethylene (PE) fibers, Constr. Build. Mater. 158 (2018) 217-227.

[8] V.C. Li, S. Wang, C. Wu, Tensile strain-hardening behavior of polyvinyl alcohol engineered cementitious composite (PVA-ECC), ACI Mater. J. 98(6) (2001) 483-492.

[9] V.C. Li, H. Horii, P. Kabele, T. Kanda, Y.M. Lim, Repair and retrofit with engineered cementitious composites, Eng. Fract. Mech. 65(2-3) (2000) 317-334.

[10] A.R. Sakulich, V.C. Li, Nanoscale characterization of engineered cementitious composites (ECC), Cem. Concr. Res. 41(2) (2011) 169-175.

[11] V.C. Li, C. Wu, S. Wang, A. Ogawa, T. Saito, Interface tailoring for strain-hardening polyvinyl alcohol-engineered cementitious composite (PVA-ECC), ACI Mater. J. 99(5) (2002) 463-472.

[12] L.-l. Kan, H.-s. Shi, Investigation of self-healing behavior of engineered cementitious composites (ECC) materials, Constr. Build. Mater. 29 (2012) 348-356.

[13] T. Kanda, T. Saito, N. Sakata, M. Hiraishi, Tensile and anti-spalling properties of direct sprayed ECC, J. Adv. Concr. Technol. 1(3) (2003) 269-282.

514 [14] Y.Y. Kim, G. Fischer, Y.M. Lim, V.C. Li, Mechanical Performance of Sprayed
515 Engineered Cementitious Composite Using Wet-Mix Shotcreting Process for Repair
516 Applications, ACI Mater. J. 101(1) (2004) 42-49.
517 [15] Z. Zhang, S. Qian, H. Ma, Investigating mechanical properties and self-healing
518 behavior of micro-cracked ECC with different volume of fly ash, Constr. Build. Mater.
519 52 (2014) 17-23.
520 [16] M. Şahmaran, V.C. Li, Influence of microcracking on water absorption and
521 sorptivity of ECC, Mater. Struct. 42 (2009) 593–603.
522 [17] M. Sahmaran, M. Li, V.C. Li, Transport properties of engineered cementitious
523 composites under chloride exposure, ACI Mater. J. 104(6) (2007) 604-611.
524 [18] G. Yildirim, M. Sahmaran, M. Balcikanli, E. Ozbay, M. Lachemi, Influence of
525 cracking and healing on the gas permeability of cementitious composites, Constr. Build.
526 Mater. 85 (2015) 217-226.
527 [19] M. Sahmaran, V.C. Li, C. Andrade, Corrosion resistance performance of steel-
528 reinforced engineered cementitious composite beams, ACI Mater. J. 105(3) (2008) 243-
529 250.
530 [20] C. Andrade, C. Alonso, F.J. Molina, Cover cracking as a function of bar corrosion:
531 Part I-Experimental test, Mater. Struct. 26(8) (1993) 453–464.
532 [21] M. Li, R. Ranade, L. Kan, V.C. Li, On improving the infrastructure service life
533 using ECC to mitigate rebar corrosion, Proceedings of 2nd International Symp. on
534 Service Life Design for Infrastructure, Delft, The Netherlands, 2010, pp. 773-782.
535 [22] K.-Q. Yu, Z.-D. Lu, J.-G. Dai, S.P. Shah, Direct Tensile Properties and Stress–
536 Strain Model of UHP-ECC, J. Mater. Civ. Eng. 32(1) (2020) ariticle: 04019334.
537 [23] K.-Q. Yu, J.-G. Dai, Z.-D. Lu, C.-S. Poon, Rate-dependent tensile properties of
538 ultra-high performance engineered cementitious composites (UHP-ECC), Cem. Concr.

539 Compos. 93 (2018) 218-234.
540 [24] J. Xu, X. Wang, Self-healing of concrete cracks by use of bacteria-containing low
541 alkali cementitious material, Constr. Build. Mater. 167 (2018) 1-14.
542 [25] Y. Goto, Cracks Formed in Concrete Around Deformed Tension Bars, In: Journal
543 Proceedings 68(4) (1971) 244-251.
544 [26] N. Otsuki, S.-i. Miyazato, W. Yodsudjai, Influence of recycled aggregate on
545 interfacial transition zone, strength, chloride penetration and carbonation of concrete, J.
546 Mater. Civ. Eng. 15(5) (2003).
547 [27] A. Litorowicz, Identification and quantification of cracks in concrete by optical
548 fluorescent microscopy, Cem. Concr. Res. 36(8) (2008) 1508-1515.
549 [28] Í.B. Silva, X-ray Computed Microtomography technique applied for cementitious
550 materials: A review, Micron 107 (2018) 1-8.
551 [29] E.E. Bernardes, E.V.M. Carrasco, W.L. Vasconcelos, A.G.d. Magalhães, X-ray
552 microtomography (μ-CT) to analyze the pore structure of a Portland cement composite
553 based on the selection of different regions of interest, Constr. Build. Mater. 95 (2015)
554 703-709.
555 [30] W. Sun, K. Hou, Z. Yang, Y. Wen, X-ray CT three-dimensional reconstruction and
556 discrete element analysis of the cement paste backfill pore structure under uniaxial
557 compression, Constr. Build. Mater. 138 (2017) 69-78.
558 [31] N. Bossa, P. Chaurand, J. Vicente, D. Borschneck, C. Levard, O. Aguerre-Chariol,
559 J. Rose, Micro-and nano-X-ray computed-tomography: A step forward in the
560 characterization of the pore network of a leached cement paste, Cem. Concr. Res. 67
561 (2015) 138-147.
562 [32] R. Qian, Y. Zhang, C. Liu, L. Yang, G. Liu, W. She, Quantitative characterization
563 of three-dimensional pore structure in hardened cement paste using X-ray

564 microtomography combined with centrifuge driven metal alloy intrusion, Mater.
565 Charact. 145 (2018) 277-283.
566 [33] B. Chen, W. Lin, X. Liu, F. Iacoviello, P. Shearing, I. Robinson, Pore structure
567 development during hydration of tricalcium silicate by X-ray nano-imaging in three
568 dimensions, Constr. Build. Mater. 200 (2019) 318-323.
569 [34] Y. Li, Y. Li, Z. Guan, Q. Ding, Elastic modulus damage model of cement mortar
570 under salt freezing circumstance based on X-ray CT scanning, Constr. Build. Mater.
571 191 (2018) 1201-1209.
572 [35] B. Dong, G. Fang, Y. Liu, P. Dong, J. Zhang, F. Xing, S. Hong, Monitoring
573 reinforcement corrosion and corrosion-induced cracking by X-ray microcomputed
574 tomography method, Cem. Concr. Res. 100 (2017) 311-321.
575 [36] G. Fang, Y. Liu, S. Qin, W. Ding, J. Zhang, S. Hong, F. Xing, B. Dong, Visualized
576 tracing of crack self-healing features in cement/microcapsule system with X-ray
577 microcomputed tomography, Constr. Build. Mater. 179 (2018) 336-347.
578 [37] L. Yang, D. Gao, Y. Zhang, W. She, Study on water and chloride transport in
579 cracked mortar using X-ray CT, gravimetric method and natural immersion method,
580 Constr. Build. Mater. 176 (2018) 652-664.
581 [38] K. Schabowicz, Z. Ranachowski, D. Jóźwiak-Niedźwiedzka, Ł. Radzik, S.K. Jr, T.
582 Dvorak, Application of X-ray microtomography to quality assessment of fibre cement
583 boards, Constr. Build. Mater. 110 (2016) 182-188.
584 [39] P. Carrara, R. Kruse, D.P. Bentz, M. Lunardelli, T. Leusmann, P. Varady, L.D.
585 Lorenzis, Improved mesoscale segmentation of concrete from 3D X-ray images using
586 contrast enhancers, Cem. Concr. Compos. 93 (2018) 30-42.
587 [40] S.-Y. Chung, M. AbdElrahman, D. Stephan, P.H. Kamm, Investigation of
588 characteristics and responses of insulating cement paste specimens with Aer solids

589 using X-ray micro-computed tomography, Constr. Build. Mater. 118 (2016) 204-215.
590 [41] Y. Alrefaei, J.-G. Dai, Tensile behavior and microstructure of hybrid fiber ambient
591 cured one-part engineered geopolymer composites, Constr. Build. Mater. 184 (2018)
592 419-431.
593 [42] Y. Alrefaei, K. Rahal, M. Maalej, Shear strength of beams made using hybrid fiber–
594 engineered cementitious composites, J. Struct. Eng. 144(1) (2018) article number:
595 04017177.
596 [43] ASTM C109, Standard Test Method for Compressive Strength of Hydraulic
597 Cement Mortars, ASTM International, West Conshohocken, PA, 2020.
598 [44] JSCE. Recommendations for Design and Construction of High Performance Fiber
599 Reinforced Cement Composites with Multiple Fine Cracks. Tokyo: Japan Society of
600 Civil Engineers; 2008. .
601 [45] ASTM C1273-05, Standard Test Method for Tensile Strength of Monolithic
602 Advanced Ceramics at Ambient Temperatures, American Society of Testing and
603 Materials, West Conshohocken, PA, 2005.
604 [46] F.A. Shaker, A.S. El-Dieb, M.M. Reda, Durability of Styrene-Butadiene latex
605 modified concrete, Cem. Concr. Res. 27(5) (1997) 711-720.
606 [47] S.H. Okba, A.S. El-Dieb, M.M. Reda, Evaluation of the corrosion resistance of
607 latex modified concrete (LMC), Cem. Concr. Res. 27(6) (1997) 861-868.
608 [48] T.A.E. Maaddawy, K.A. Soudki, Effectiveness of impressed current technique to
609 simulate corrosion of steel reinforcement in concrete, J. Mater. Civ. Eng. 15(1) (2003)
610 41-47.
611 [49] P. Iassonov, T. Gebrenegus, M. Tuller, Segmentation of X-ray computed
612 tomography images of porous materials: A crucial step for characterization and
613 quantitative analysis of pore structures, Water Resour. Res. 45(9) (2009) article number:

614 W09415.
615 [50] M.D. Lepech, V.C. Li, Large-scale processing of engineered cementitious
616 composites, ACI Mater. J. 105(4) (2008) 358-366.
617 [51] S. Sasmal, G. Avinash, Investigations on mechanical performance of cementitious
618 composites micro-engineered with poly vinyl alcohol fibers, Constr. Build. Mater. 128
619 (2016) 136-147.
620 [52] T. Kanda, V.C. Li, Interface property and apparent strength of a high strength
621 hydrophilic fiber in cement matrix, J. Mater. Civ. Eng. 10(1) (1998) 5-13.
622 [53] B.-T. Huang, J. Yu, J.-Q. Wu, J.-G. Dai, C.K. Leung, Seawater sea-sand Engineered
623 Cementitious Composites (SS-ECC) for marine and coastal applications, Compos.
624 Commun. 20 (2020) aritile number: 100353.
625 [54] I. Balafas, C.J. Burgoyne, Modeling the structural effects of rust in concrete cover,
626 J. Eng. Mech. 137(3) (2011) 175-185.
627 [55] K. Bhargava, A.K. Ghosh, Y. Mori, S. Ramanujam, Analytical model for time to
628 cover cracking in RC structures due to rebar corrosion, Nucl. Eng. Des. 236(11) (2006)
629 1123-1139.
630 [56] Y. Zhao, J. Yu, Y. Wu, W. Jin, Critical thickness of rust layer at inner and out surface
631 cracking of concrete cover in reinforced concrete structures, Corrosion Sci. 59 (2012)
632 316-323.
633 [57] W.A. Tasong, C.J. Lynsdale, J.C. Cripps, Aggregate-cement paste interface. ii:
634 influence of aggregate physical properties, Cem. Concr. Res. 28(10) (1998) 1453-1465.
635 [58] M. Nili, A. Ehsani, Investigating the effect of the cement paste and transition zone
636 on strength development of concrete containing nanosilica and silica fume, Mater. Des.
637 75 (2017) 174-183.
638 [59] L. Hou, H. Liu, S. Xu, N. Zhuang, D. Chen, Effect of corrosion on bond behaviors

639 of rebar embedded in ultra-high toughness cementitious composite, Constr. Build.
640 Mater. 138 (2017) 141-150.
641 [60] J. Sauvola, M. Pietikäinen, Adaptive document image binarization, Pattern
642 Recognit. 33(2) (2000) 225-236.
643 [61] Y.-S. Wang, J.-G. Dai, X-ray computed tomography for pore-related
644 characterization and simulation of cement mortar matrix, NDT E Int. 86 (2017) 28-35.
645 [62] O. Rozenbaum, S.R.d. Roscoat, Representative elementary volume assessment of
646 three-dimensional x-ray microtomography images of heterogeneous materials:
647 Application to limestones, Phys. Rev. E 89 (2014) article number: 053304.
648 [63] A. Almhdie, O. Rozenbaum, E. Lespessailles, R. Jennane, Image processing for
649 the non-destructive characterization of porous media. Application to limestones and
650 trabecular bones, Math. Comput. Simul. 99 (2014) 82-94.
651